



Cite this: *New J. Chem.*, 2019, 43, 16305

Aggregation-induced emission based PET probe for liver function imaging†

Song Liu,^a Yong Huang,^a Yajing Liu,^b Renbo Wu,^a Zequn Yang,^a Yuli Sun,^a Hao Xiao,^a Xuebo Cheng^a and Zehui Wu^{id}*^a

To locate the site of a liver lesion by positron emission tomography (PET) imaging and then remove the lesion site under the guidance of fluorescence imaging, we designed an aggregate-induced emission (AIE)-based PET probe [^{nat/68}Ga] **5** based on the effects of the reticuloendothelial system. By modifying derivatives of tetraphenylethene, we obtained a bifunctional chelating agent with AIE characteristics, which can complex with ^{nat}Ga³⁺ or ⁶⁸Ga³⁺ at room temperature to form [^{nat}Ga] **5** or [⁶⁸Ga] **5**. [^{nat}Ga] **5** has typical AIE characteristics and can form nanomicelles when its concentration is greater than the critical micelle concentration (CMC). Cellular fluorescence confocal imaging experiments and radioactive uptake experiments showed that Kupffer cells had a high uptake of [^{nat/68}Ga] **5** while HepG2 cells had lower uptake of [^{nat/68}Ga] **5**, indicating that liver function imaging was achieved by the phagocytosis of [^{nat/68}Ga] **5** by Kupffer cells into the liver. A biodistribution study showed that [⁶⁸Ga] **5** shows high accumulation in the liver after intravenous injection into rats. The *in vivo* PET imaging profile demonstrated an excellent liver to muscle ratio. Thus, [^{nat/68}Ga] **5** could potentially be used as a liver function PET imaging agent for clinical diagnosis and intraoperative navigation.

Received 3rd September 2019,
Accepted 29th September 2019

DOI: 10.1039/c9nj04537f

rsc.li/njc

1. Introduction

The liver is the largest gland in the human body and is an organ mainly characterized by metabolism. The liver plays a very important role in human metabolism, bile production, detoxification, coagulation, immunity, heat production and regulation of water and electrolytes.¹ There are many diseases associated with the liver, including viral and non-viral hepatitis, cirrhosis, alcoholic liver disease, autoimmune liver disease, non-alcoholic fatty liver disease and liver cancer. Most liver diseases are occult and the early clinical symptoms are not obvious; therefore, diseases are often found in the late stages of cirrhosis and liver cancer.^{2–4} Liver tumour resection and liver transplantation are the main methods for curing liver cancer.^{5,6} Accurate evaluation of liver function before surgery is expected to be the most important factor for the safe resection of the liver and accurate assessment of postoperative residual liver function.⁷ Therefore, the detection of liver function by high-sensitivity imaging technology is of great significance for the diagnosis, treatment and prognosis of liver disease, especially liver cancer. Various imaging methods have been developed, including ultrasound imaging,⁸ computed

tomography (CT),⁹ magnetic resonance imaging (MRI),¹⁰ single photon emission computed tomography (SPECT)¹¹ and positron emission tomography (PET).^{12,13} Each of these imaging modalities has its own advantages and disadvantages, and it requires comprehensive consideration to achieve a three-dimensional qualitative/quantitative assessment of liver function.¹⁴ Accordingly, attempts have been made to overcome their respective shortcomings and are driving the ongoing efforts to develop dual modality imaging instruments and contrasts so that the advantages of these techniques can be synergistically combined to provide accurate physiological and anatomical information. In the past few years, different strategies have been applied to achieve multimodal liver function imaging, such as reports of MRI-FL liver imaging agents.¹⁵

PET can be non-invasive, highly sensitive, and highly specific for the quantitative determination of functional liver mass for patient management in a variety of clinical settings, including liver surgery and transplantation as well as the diagnostic and therapeutic monitoring of cancer.^{12,13} However, its spatial resolution is very poor (≥ 1 cm for a clinical scanner). Fluorescence imaging (FL) has high sensitivity and high spatial resolution,¹⁶ which complements the shortcoming of PET. Therefore, a PET-FL bimodal liver function imaging agent can evaluate the function of the liver and locate the tumour or liver necrosis according to PET imaging and then accurately remove the tumour or liver necrosis site under the guidance of fluorescence imaging.

^a Brain Institute of Brain Disorders, Capital Medical University, Beijing 100069, China. E-mail: wzhhuey2012@ccmu.edu.cn

^b School of Pharmaceutical Science, Capital Medical University, Beijing 100069, China

† Electronic supplementary information (ESI) available. See DOI: 10.1039/c9nj04537f

The development of PET-FL probes for liver function imaging is more challenging than single modality agents.^{17,18} These probes usually consist of fluorophores, linkers, radionuclides and their complexing agents, and targeting molecules, each of which plays a very important role in imaging.¹⁹ Additionally, fluorophores experience some effects from emission quenching, either partially or completely in many conventional systems.²⁰ The harsh conditions of radiolabelling can result in changes to the molecular structure of the target molecule.²¹ Complex agents or fluorophores can affect the affinity of the probe for the target. Therefore, to solve the above problems, a novel strategy for designing dual-mode imaging agents for PET-FL is particularly important for the development of new imaging probes.

Compared with the traditional PET-FL bimodal imaging probes consisting of five units, a new strategy attempts to integrate the fluorophore, nuclides and complexing agents into one unit in this paper. Fluoregens bearing aggregate-induced emission (AIE) characteristics have been introduced into dual-mode imaging probes in new strategies to overcome conventional aggregation-caused quenching (ACQ), which has been extensively studied in optoelectronic devices, chemical and biosensors, bioimaging, *etc.*^{15,22–33} AIE, conceptually termed by Tang in 2001,³⁴ can actively utilize luminogen aggregation to enhance its emissions. Tetraphenylethene (TPE) is one of the most famous AIE fluorogens,²² and by structural modification, its amphiphilic derivatives have been shown to act as a good chelating agent to label $^{68}\text{Ga}^{3+}$, a useful PET radionuclide with a 68 min half-life and mild labelling conditions.³⁵ Thus, the integration of fluorophores, nuclides and complexing agents into amphiphilic TPE derivatives reduces the difficulty of design and links to different targeting molecules to develop dual-mode PET-FL imaging probes for the diagnosis of different diseases. The amphiphilic $^{\text{nat}}\text{Ga}^{3+}$ or $^{68}\text{Ga}^{3+}$ complex may form nanomicelles larger than 100 nm at a suitable concentration, which in turn can be specifically and mainly trapped in the macrophages of the reticuloendothelial system (RES).¹⁵ Kupffer cells located in the liver are specialized macrophages that act as an integral part of the sinusoids. The Kupffer cells can remove the PET-FL probe from the bloodstream through the phagocytosis pathway, resulting in the accumulation of the PET-FL probe in the liver tissue, which in turn allows liver function imaging.

To obtain the PET-FL liver function imaging agent, we synthesized a bifunctional chelating agent with AIE characteristics that can complex with $^{\text{nat}}\text{Ga}^{3+}$ or $^{68}\text{Ga}^{3+}$ at room temperature to form [$^{\text{nat}}\text{Ga}/^{68}\text{Ga}$] **5**. Because of the formation of nanoaggregates, [^{68}Ga] **5** displays high liver uptake in rats with an excellent liver to muscle ratio. The utilization of [$^{\text{nat}}\text{Ga}$] **5** for cell imaging was examined, and the feasibility of using [^{68}Ga] **5** as a PET imaging agent was demonstrated.

2. Experimental

2.1 Materials

All reagents were commercial products used without further purification unless otherwise indicated. Deionized water used in our experiments was obtained from a Milli-Q water system. Kupffer cell and HepG2 cell were obtained from the American,

ATCC, Manassas, VA. Fetal bovine serum were purchased from Beijing YuanHeng ShenMa Biology Technology Research Institute. Culture medium and 3-(4,5-dimethylthiazol-2-yl)-2,5-diphenyl-tetrazolium bromide (MTT) were purchased from Sigma.

2.2 Instruments

NMR spectra were recorded at 300 MHz at ambient temperature. Chemical shifts are reported in parts per million downfield from TMS (tetramethylsilane). Coupling constants in ^1H NMR are expressed in Hertz. High-resolution mass spectrometry (HRMS) data was obtained with an Agilent (Santa Clara, CA) G3250AA LC/MSD TOF system. Thin-layer chromatography (TLC) analysis were performed using Merck (Darmstadt, Germany) silica gel 60 F254 plates. Crude compounds were generally purified by flash column chromatography (FC) packed with Teledyne ISCO. Photoluminescence (PL) spectra were recorded on a F-2500 spectrofluorometric Hitachi, Ltd. The morphology of **5** aggregates was investigated using transmission electron microscopy (TEM; Japan, JEM-2100) at an accelerating voltage of 100 kV. Dynamic light scattering (DLS) and zeta potential measurements were performed on a Malvern Zetasizer Nano-ZS90. For cell imaging experiments, Kupffer cells and HepG2 cells were imaged under a Zeiss LSM-880 confocal laser scanning microscope (Zeiss, Germany). $^{68}\text{Ge}/^{68}\text{Ga}$ generator supplied by Isotope Technologies Garching (ITG), Germany. For cytotoxicity experiments, cells were treated with MTT and the absorbance was measured on a 1420 Victor Multi-Label Counter (PerkinElmer Life Science). Small animal PET imaging data were recorded on a microPET (Inveon, Siemens, Germany, Detector Type: LSO with 1.6×1.6 mm detector pixel spacing; Spatial Resolution: 1.4 mm).

2.3 Synthesis

2,2'-((Ethane-1,2-diylbis(azane diyl))bis(methylene))bis(4-(1,2,2-triphenylvinyl)phenol) (2). A solution of **1** (0.69 g, 2 mmol) was added in 20 mL methanol at room temperature, ethane-1,2-diamine (60 mg, 1 mmol) were added. The solution was stirred at 60 °C for 3 h. NaBH_4 (0.14 g, 4 mmol) was added above solution in portions at 0 °C for 1 h. The reaction was then acidified with 1 M HCl until the pH = 7 under cooling with ice bath. The methanol was removed and water phase was extracted with ethyl acetate (20 mL \times 3). The organic phases were combined, washed with Sat. NaHCO_3 (20 mL) and brine (20 mL), and dried with MgSO_4 . The filtrate was evaporated and extracted by ethyl acetate, dried by Na_2SO_4 , purified by FC (DCM/methanol = 10/1) to give **2** (0.43 g, 56.1%) as white solid. ^1H NMR (300 MHz, CDCl_3) δ 7.11–7.03 (m, 30H), 6.83 (d, J = 7.5 Hz, 2H), 6.73–6.48 (m, 4H), 3.73 (s, 4H), 2.60 (s, 4H). ^{13}C NMR (75 MHz, CDCl_3) δ 156.64, 144.28, 144.17, 143.87, 140.33, 139.60, 134.71, 131.96, 131.75, 131.40, 131.33, 127.58, 126.35, 126.18, 126.08, 121.22, 115.46, 100.07, 77.43, 77.01, 76.59, 51.98, 47.37. HRMS calcd for $\text{C}_{56}\text{H}_{48}\text{N}_2\text{O}_2$ 780.3716; found, 781.3632 [$\text{M} + \text{H}$] $^+$.

Di-tert-butyl 2,2'-(ethane-1,2-diylbis((2-hydroxy-5-(1,2,2-triphenylvinyl)benzyl)azanediyl))diacetate (3). A solution of **2** (0.4 g, 0.51 mmol) and K_2CO_3 (0.28 g, 2 mmol) were added in 45 mL acetonitrile was stirred at room temperature for 0.5 h, *t*-butyl 2-bromoacetate (190 mg, 1 mmol) was added. The reaction was

stirred at 60 °C for overnight. The reaction was filtered and evaporated *in vacuo*, purified by FC (hexane/ethyl acetate = 4/1) to give **3** (0.24 g, 46.7%) as white solid. ^1H NMR (300 MHz, DMSO) δ 9.54 (s, 1H), 7.17–7.01 (m, 18H), 6.95–6.90 (m, 12H), 6.67 (d, J = 6.4 Hz, 4H), 6.52 (d, J = 8.8 Hz, 2H), 3.42 (s, 4H), 3.03 (s, 4H), 2.35 (s, 4H), 1.39 (s, 18 H). ^{13}C NMR (75 MHz, DMSO) δ 170.62, 155.69, 144.20, 143.96, 143.83, 141.06, 139.72, 134.12, 131.14, 128.18, 128.08, 126.83, 126.59, 122.70, 115.36, 80.97, 55.34, 40.87, 40.59, 40.32, 40.04, 39.76, 39.48, 39.20, 28.23. HRMS calcd for $\text{C}_{68}\text{H}_{68}\text{N}_2\text{O}_6$ 1008.5077; found, 1009.4784 $[\text{M} + \text{H}]^+$.

2,2'-(Ethane-1,2-diylbis((2-hydroxy-5-(1,2,2-triphenylvinyl)benzyl)-azanediyl)diacetic acid (4). A solution of **3** (100 mg, 0.099 mmol) and trifluoroacetic acid (TFA, 4 mL) was stirred at room temperature for 3 h. The solvent was removed under vacuum, diethyl ether was added, washed by diethyl ether, white solid **4** was collected (89 mg, 100%). ^1H NMR (300 MHz, DMSO) δ 7.06 (s, 18H), 6.99–6.88 (m, 12H), 6.67 (s, 4H), 6.54 (s, 2H), 3.43 (s, 4H), 3.08 (s, 4H), 2.40 (s, 4H). ^{13}C NMR (75 MHz, DMSO) δ 172.77, 155.76, 144.18, 143.98, 143.85, 140.94, 139.73, 134.12, 131.64, 131.16, 128.17, 128.10, 126.85, 126.69, 122.15, 115.46, 67.45, 55.34, 54.19, 40.82, 40.54, 40.26, 39.98, 39.70, 39.43, 39.15. HRMS calcd for $\text{C}_{60}\text{H}_{52}\text{N}_2\text{O}_6$ 896.3825; found, 897.3557 $[\text{M} + \text{H}]^+$.

Gallium N-(2-((carboxylatomethyl)(2-hydroxy-5-(1,2,2-triphenylvinyl)benzyl)amino)ethyl)-N-(2-oxido-5-(1,2,2-triphenylvinyl)benzyl)-glycinate (5). A solution of **4** (100 mg, 0.11 mmol) and GaCl_3 (0.19 g, 1.1 mmol) was stirred in 0.5 mL DMSO and 0.5 mL H_2O at room temperature for overnight. The reaction was purified by semi-HPLC and afforded white solid **5** (95 mg, 89.2%). ^1H NMR (300 MHz, DMSO) δ 7.26–6.86 (m, 30H), 6.55 (dd, J = 8.5, 2.3 Hz, 2H), 6.38 (d, J = 2.2 Hz, 2H), 6.28 (d, J = 8.5 Hz, 2H), 3.17–3.13 (m, 2H), 3.01–2.95 (m, 3H), 2.77–2.72 (m, 7H). ^{13}C NMR (75 MHz, DMSO) δ 171.58, 163.13, 144.69, 144.31, 143.06, 141.47, 138.12, 133.78, 132.12, 131.82, 131.40, 131.30, 131.14, 129.26, 128.23, 128.11, 128.01, 126.70, 126.41, 119.96, 99.99, 60.99, 56.14, 55.33, 41.98. HRMS calcd for $\text{C}_{60}\text{H}_{49}\text{GaN}_2\text{O}_6$ 962.2846; found, 963.2499 $[\text{M} + \text{H}]^+$.

2.4 Radiosynthesis of ^{68}Ga **5**

0.2 mL eluent in 0.05 M HCl of $^{68}\text{Ge}/^{68}\text{Ga}$ generator (ITG, Germany) and 0.2 mL 2 N HEPES (pH = 7) were added and mixed with 10 μL of $4 \times 10^{-3} \text{ mol L}^{-1}$ and reacted at room temperature for 10 min (Scheme S1, ESI †). Labeling efficiency and radiochemical purity were determined using Radio-HPLC. Radiochemical purity of ^{68}Ga **5** was > 95%. Therefore, the tracer was diluted and used *in vitro* and *in vivo* experiments without further purification. Analytical reversed-phase high performance liquid chromatography (RP-HPLC) was performed on a Gemini-NX 5u C18 110A column (150 \times 4.6 mm) using an Agilent gradient HPLC System. The ^{68}Ga **5** was eluted applying gradients of in 0.1% TFA in H_2O and acetonitrile (ACN) at a constant flow of 1 mL min^{-1} (0–2 min, 10%ACN; 2–30 min, 10–60% ACN; 20–21 min, 60% ACN; 20–26 min, 100% ACN). ^{68}Ga **5** had retention times of 23.6 min (Fig. 1a).

2.5 Cell culture and imaging

Kupffer cells were cultured in RPMI 1640 (SIGMA) supplemented with 10% fetal bovine serum (YHSM) and 1% penicillin/streptomycin (Gibco). HepG2 cells were cultured in DMEM/HIGH

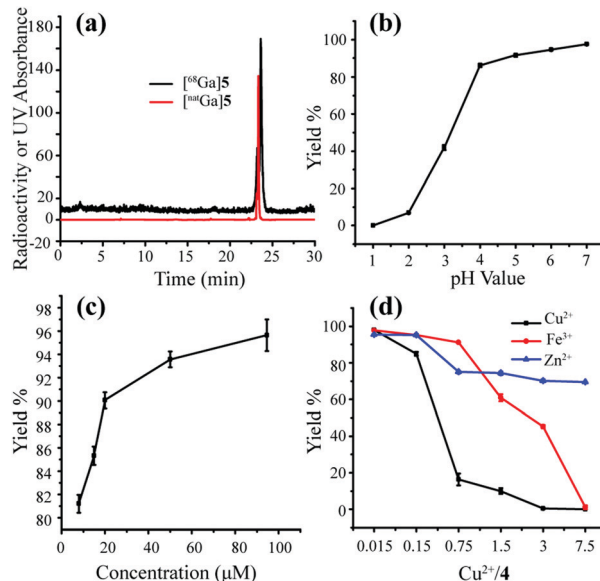


Fig. 1 (a) HPLC profiles of ^{nat}Ga **5** and ^{68}Ga **5** using the following system (column: Gemini-NX 5u C18 110A (150 \times 4.6 mm), mobile phase ACN/0.1% TFA in H_2O , 1 mL min^{-1} (0–2 min, 10% ACN; 2–30 min, 10–60% ACN; 20–21 min, 60–100% ACN; 20–26 min, 100% ACN), and column temperature of 30 °C). ^{nat}Ga **5** and ^{68}Ga **5** had retention times of 23.3 and 23.6 min, respectively. Labelling yield of ^{68}Ga **5** in HEPES buffer 100 °C at (b) different pH values, (c) concentrations and (d) concentrations of metal cations. Each data point represents the mean \pm SD from triplicate trials.

GLUCOSE (HyClone) supplemented with 10% fetal bovine serum (YHSM) and 1% penicillin/streptomycin (Gibco). The cells were maintained in T-75 culture flasks under humidified incubator conditions (37 °C, 5% CO_2) and were routinely passaged at confluence. Cells were plated (1.0×10^5 cells per well) overnight in the media prior to ligand incubation. ^{nat}Ga **5** was dissolved in DMSO with the concentration of 10 mM as stock solution. For cell imaging, Kupffer cells and HepG2 cells were seeded overnight on a coverslip mounted onto a 35 mm Petri dish and then stained with different concentrations ^{nat}Ga **5**.

2.6 Cell uptake of ^{68}Ga **5**

The cells were cultured for 2 days at 37 °C in a 5% CO_2 incubator. Each cell line was set at four time points of 5, 30, 60 and 120 min, and four replicate wells were set at each time point. The well plates were removed, the medium was washed away, and each well was washed three times with 1 mL of pre-heated PBS in 37 °C (containing Ca^{2+} and Mg^{2+}). Add 1 mL of PBS-configured 37 KBq (1 μCi) ^{68}Ga **5** to each well and place in a 37 °C incubator. The plates were removed after four time points, PBS was aspirated and washed three times with 1 mL of cold PBS without Ca^{2+} and Mg^{2+} . The cells were harvested; the radioactivity was counted by adding a gamma counter.

2.7 In vitro stability in PBS and plasma

^{68}Ga **5** was added to 0.1 M phosphate buffered saline (PBS, pH = 7.0) or rat plasma, and the solutions were incubated at 37 °C for 30, 60 and 120 min. Plasma was filtered through a

filter (0.22 μm) and radiochemical purity of the filtrate was analyzed by RP-HPLC. The RCP was measured and analyzed by the radio-HPLC to determine the stability of [^{68}Ga] **5** as a function of time.

2.8 Cell proliferation assay

Kupffer cells were seeded into a 96-well plate at a density of 3000 cells per well and incubated for 12 h at 37 $^{\circ}\text{C}$ and 5% CO_2 in culture medium. The cells were washed with 0.1 mL \times PBS. Then different concentrations of [^{68}Ga] **5** and fresh culture medium were added. After 24 h incubation, all cells were then exposed to 20 μL of a MTT solution (5 mg mL^{-1}). After 4 h at 37 $^{\circ}\text{C}$, culture media was removed and 0.15 mL dimethyl sulfoxide was added. The absorbance of individual wells at 570 nm was measured on a 1420 Victor Multi-Label Counter. All experiments were repeated three times.

2.9 *In vivo* autoradiography and fluorescence imaging of liver sections

For *in vivo* autoradiographic studies, Healthy BALB/c mice (18–22 g, purchase from Beijing Charles river Laboratories). All animal procedures were performed in accordance with the Guidelines for Care and Use of Laboratory Animals of Capital Medical University and experiments were approved by the Animal Ethics Committee of Capital Medical University. Studies of the *in vitro* autoradiography and fluorescence imaging of [^{68}Ga] **5** was performed in mice. Approximately 1.29 MBq [^{68}Ga] **5** was administered *via* the tail vein in conscious animals. At 60 min postinjection, the mice were sacrificed under anesthesia. The liver was rapidly removed, placed in a Tissue-Tek OCT compound (Sakura, Japan), and frozen in a dry ice–acetone bath for 2 h. After reaching equilibrium to -20 $^{\circ}\text{C}$, 35 μm sections were consecutively cut by a cryostat microtome (Leica, CM1950, GER), thaw mounted on gelatin-coated microscope slides, and air-dried at room temperature. The slides were then exposed to a phosphor screen (PerkinElmer Cyclone plus, C431200, USA) in an autoradiographic cassette for 20 h. The autoradiography images were acquired through a Typhoon FLA 7000 (Perkin-Elmer Cyclone plus, C431200, USA). The fluorescence images were acquired through Panoramic scan (3DHitech II, Hungary).

2.10 Biodistribution studies in rats

Healthy male Sprague Dawley rats (180–220 g, purchase from Beijing Charles river Laboratories) were injected with [^{68}Ga] **5** (740 KBq, 0.1 mL) through a tail vein under anesthesia with 2% isoflurane. The injected mice were sacrificed at 5, 30, 60 and 120 min postinjection. Brain, blood, liver, muscle, kidney, lung, heart, skin, bone and spleen were then excised, blotted, and weighed, and then ^{68}Ga radioactivity of each organ was counted by a gamma scintillation counter. Results were expressed as the percentage of injected dose per gram of tissue (% ID per g). The percent dose per gram to brain ratios was calculated by a comparison of the tissue activity counts to counts of 1% of the initial dose.

2.11 MicroPET imaging

Dynamic PET/CT imaging studies were conducted in healthy male Sprague Dawley rats. Rats were anesthetized using 2%

isoflurane in oxygen at 2 L min^{-1} , in an induction chamber. When fully anesthetized, the animals were placed on the scanner bed, with a nose cone used to maintain anesthesia at 1% isoflurane in oxygen at 2 L min^{-1} . Body temperature was maintained at 37 $^{\circ}\text{C}$ by using a water-circulated pad under the animals. Immediately after the start of the scan, a dose of radio tracer (~ 300 μCi , 11.1 MBq) was injected *via* the tail vein. The animals were visually monitored for breathing and any other signs of distress throughout the entire imaging period. All scans were conducted over a period of 120 min (dynamic, 5 min per frame). Regions of interest (ROIs) were drawn over liver guided by CT images using Amira 3.1 image visualization and analysis software. Radioactivity within the ROIs of each frame was calculated. The radioactivity in the liver ROI for each frame was decay-corrected. The time–activity curve of liver was plotted from the liver ROI activities in each frame.

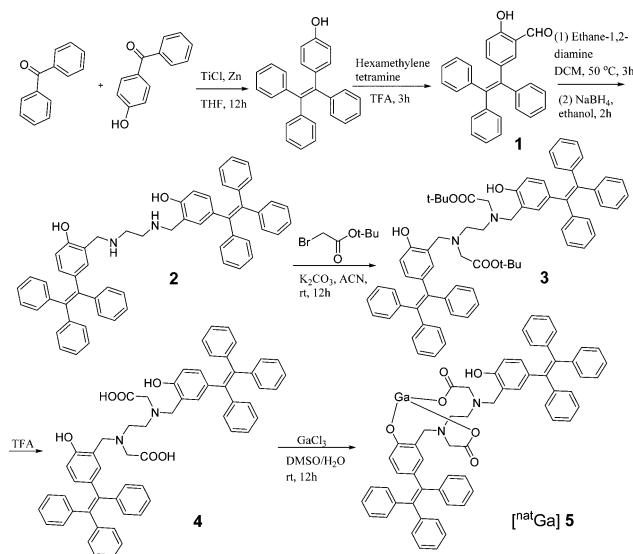
2.12 Statistical analysis

Data were presented as mean \pm standard deviation (SD). All statistical tests were conducted using the IBM SPSS Statistics Version 20.0 for Windows (SPSS, Inc., IBM Company). The independent samples nonparametric test was used to compare the difference of two quantitative groups. Pearson product-moment correlation coefficient (r) was used for correlation analysis between continuous variables. A P value of less than 0.05 was considered statistically significant.

3. Results and discussion

3.1 Synthesis and characterization of [^{68}Ga] **5**

To enable the TPE derivative to efficiently complex $^{68}\text{Ga}^{3+}$, [^{68}Ga] **5** was designed in accordance with the structure of HBED-CC (Scheme 1).³⁶ Intermediate **1** was prepared by the reported conditions. Condensation of **1** with ethylenediamine produced the Schiff base without need for further purification.



Scheme 1 Synthetic route to dual-modal [^{68}Ga] **5**.

The corresponding secondary amine **2** was obtained from the Schiff base after a reduction reaction with sodium borohydride in 56.1% yield. The secondary amine, **2**, was then reacted with two equivalents of *t*-butyl bromoacetate to give **3** in 46.7% yield. The *tert*-butyl group of **3** was then removed with trifluoroacetic acid (TFA) to afford **4**, in 100% yield. Gratifyingly, the desired [⁶⁸Ga] **5** was afforded by the reaction of **4** with Ga³⁺ at room temperature in 89.2% yield. All compounds were confirmed by NMR and HRMS.

3.2 Radiosynthesis and characterization of [⁶⁸Ga] **5**

The initial conditions for the [⁶⁸Ga] **5** labelling were in reference to the optimal conditions for HBED-CC labelling (total volume of 300 μL at pH = 4.0 with a concentration of **4** of 20 μM),³⁶ but the temperature was 100 °C to ensure that the **4** was fully reacted and the labelled product [⁶⁸Ga] **5** was confirmed by radio-HPLC (Scheme S1 (ESI[†]) and Fig. 1a). Gratifyingly, [⁶⁸Ga] **5** can be obtained by the above conditions, with a labelling yield of 95% and a radiochemical purity of >95%. Further detailed studies aim to determine the optimal conditions for the radiosynthesis of **4** by varying the pH value, temperature, time and concentration based on the optimized initial reaction conditions. When the pH was increased from 1 to 4, the yield of [⁶⁸Ga] **5** greatly increased, and a slight improvement in yield was observed at pH 5–7 (Fig. 1c). At pH = 7, [⁶⁸Ga] **5** can still be obtained in 95% yield at room temperature after 10 min. As the concentration increased from 8 μM to 90 μM, the labelling yield increased correspondingly under the same reaction conditions (Fig. 1b). Further investigation of the reaction time showed that when the reaction time exceeds 5 min, the labelling yield can be greater than 90% at room temperature. According to the above experimental results, the optimal labelling conditions were obtained; that is, the reaction solution was in an acetate buffer at a pH of 5–7, the concentration of **4** was not less than 20 μM, and the reaction was carried out for 5–15 min at room temperature. When the reaction solution was changed from acetic acid buffer solution to HEPES buffer solution, the above optimal conditions still apply. The effects of metal ions with ionic radii similar to Ga³⁺, such as Fe³⁺, Zn²⁺, and Cu²⁺, on ⁶⁸Ga³⁺ labelling were also investigated. The results show that Cu²⁺ had the greatest influence on the labelling, as an equivalent amount of Cu²⁺, Fe³⁺ or Zn²⁺ was added to the reaction solution and the labelling yield reduced from 95% to 20%, 60% and 70%, respectively (Fig. 1d).

3.3 AIE properties of [^{nat}Ga] **5**

After confirming the structure of [^{nat}Ga] **5**, we studied its photo-physical properties. [^{nat}Ga] **5** is weakly fluorescent when the water fraction (*f_w*) in the DMSO/water mixture is less than 60% at 330 nm excitation. As the amount of water increases, the fluorescence of the solution gradually increases, showing a typical AIE effect (Fig. 2a). The labelling precursor **4** has AIE characteristics similar to [^{nat}Ga] **5** in a mixed solvent of DMSO and water (Fig. S1, ESI[†]). It has been reported that metal complexes of amphiphilic tetraphenylethene may form micelles.¹⁵ Therefore, we speculate that [^{nat}Ga] **5** can also form micelles above a CMC. We attempted to estimate the CMC of [^{nat}Ga] **5** based on the fluorescence intensity of different concentrations of [^{nat}Ga] **5**

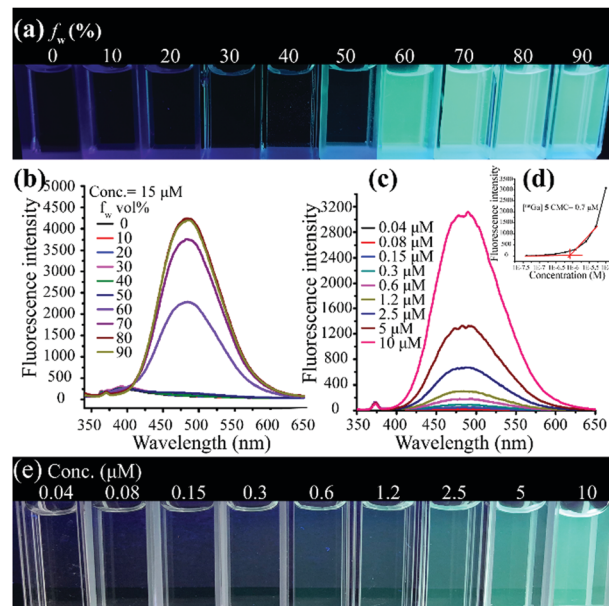


Fig. 2 (a) Photographs taken under UV irradiation and (b) emission spectra of [^{nat}Ga] **5** in aqueous solutions at different ratios of DMSO and water. Concentration of [^{nat}Ga] **5**: 15 μM. (c) Emission spectra and (e) photographs taken under UV irradiation of [^{nat}Ga] **5** in aqueous solutions at different concentrations. (d) Plots of PL intensity versus concentration of [^{nat}Ga] **5** in DMSO/H₂O = 1/99. The CMC of [^{nat}Ga] **5** is 0.7 μM. Slit width = 5 nm, excitation wavelength: 330 nm.

(Fig. 2d). Two lines are generated by analysing the relationship between the fluorescence intensity and the concentration of [^{nat}Ga] **5**, the intersection of which gives the CMC of 1 μM (Fig. 2d). Using the same method, the CMC value of **4** was determined to be 3.5 μM (Fig. S2, ESI[†]). Comparing the CMC values of **4** and [^{nat}Ga] **5**, the value of [^{nat}Ga] **5** is lower probably because of the increasing repulsive forces of the hydrophilic end helping to form micelles at low concentrations. The size and morphology of the micelle size formed by the aggregation of [^{nat}Ga] **5** was further verified by a zeta potential particle size analyser and transmission electron microscopy. Transmission electron microscopy (TEM) images show that the nanomicelles were non-uniform, easily adhesive spheres with an average diameter of approximately 55 nm (Fig. 3b), which is consistent with the hydrodynamic size measured by the zeta potential particle size analyser (Fig. 3a).

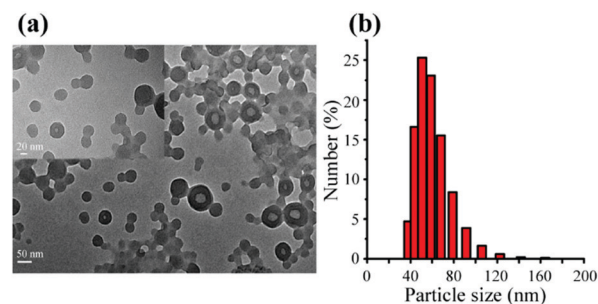


Fig. 3 (a) Transmission electron micrographs and (b) particle size analysis of [^{nat}Ga] **5** in DMSO/H₂O (10 μM).

3.4 *In vitro* fluorescent imaging of [^{nat}Ga] 5

To explore the applications of [^{nat}Ga] 5 in liver function imaging, we first tested its potential toxicity to Kupffer cells using the methyl thiazolyl tetrazolium (MTT) assay. After incubation with [^{nat}Ga] 5 at various concentrations for 24 h, no significant cell cytotoxicity from [^{nat}Ga] 5 was observed even at high concentrations up to 10 μM, which is five times higher than the working concentration in cell imaging experiments, and the cell viability was still approximately 85.2% (Fig. 5a). To further explore the mechanism of liver function imaging and the scope of the imaging applications, *in vitro* cell confocal imaging experiments were performed. Kupffer cells and HepG2 cells were incubated with [^{nat}Ga] 5 for different periods of time. As shown in Fig. 4, [^{nat}Ga] 5 illuminates the Kupffer cell membrane for approximately

10 min, while under the same conditions, [^{nat}Ga] 5 fails to induce luminescence on the HepG2 cell membrane (Fig. 4). As the incubation time increased, [^{nat}Ga] 5 further induced luminescence on the Kupffer cell membrane (Fig. 4), while [^{nat}Ga] 5 still failed to illuminate the HepG2 cell membrane. The above results indicate that the possible mechanism of [^{nat/68}Ga] 5 liver function imaging is mainly achieved by [^{nat/68}Ga] 5 engulfing the Kupffer macrophages cell.

3.5 *In vitro* stability in PBS and plasma

The *in vitro* stability of [⁶⁸Ga] 5 was investigated by incubation both in PBS and in rat plasma at 37 °C. After 2 h of incubation, the radiochemical purity was unchanged, maintaining a stable level of approximately >90% (Fig. 5b). [⁶⁸Ga] 5 was stable in plasma and PBS *in vitro* without any measurable decomposition. The release of ⁶⁸Ga³⁺ from the complex was not observed under the respective experimental conditions in the examined time frame.

3.6 Cell uptake of [⁶⁸Ga] 5

To further explore the mechanism of [⁶⁸Ga] 5 liver function imaging and verify the results of the confocal cell imaging, radioactive cell uptake experiments were performed. As shown in Fig. 5c, Kupffer cells showed higher uptake of [⁶⁸Ga] 5, increasing by 1.25%, 2.18%, 3.13% and 6.24% at 5, 30, 60 and 120 min, respectively. The uptake of [⁶⁸Ga] 5 by HepG2 cells was lower at the different time points. Based on the *in vitro* fluorescence imaging experiments, [⁶⁸Ga] 5 could be used to discriminate between Kupffer cells and HepG2 cells.

3.7 *In vivo* autoradiography and fluorescence imaging of liver sections

To realize precise image-guided resection for liver necrosis or liver tumours, it is key to ensure that the full outline of liver necrosis or liver tumours of various sizes can be visualized during the surgical process. Therefore, we attempted to co-localize normal liver tissue by fluorescence and autoradiography. As shown in Fig. 5d, the liver margin can be readily distinguished by fluorescence imaging. The liver profile detected by fluorescence imaging exhibited consistency with that of the autoradiography results (Fig. 5e). It can be seen from the experimental results that the lesion points of the liver are first found by PET imaging, and the liver necrotic tissue is removed under the guidance of fluorescence imaging.

3.8 Biodistribution studies in rats

To further investigate the pharmacokinetics of [⁶⁸Ga] 5 in rats, biodistribution experiments were performed. The results of the biodistribution studies with rats 5, 30, 60 and 120 min post-injection are shown in Table 1. [⁶⁸Ga] 5 showed a very fast accumulation throughout the entire liver with low background activity in all other organs and a very fast blood clearance (Table 1). The liver uptake of [⁶⁸Ga] 5 was rapid with $13.21 \pm 3.27\%$ ID per g at 5 min and remained relatively constant over the course of the study to $14.49 \pm 2.3\%$ ID per g at 30 min and $16.37 \pm 0.69\%$ ID per g at 60 min (Table 1). After 2 h, the liver uptake continued to increase to $20.65 \pm 2.2\%$ ID per g.

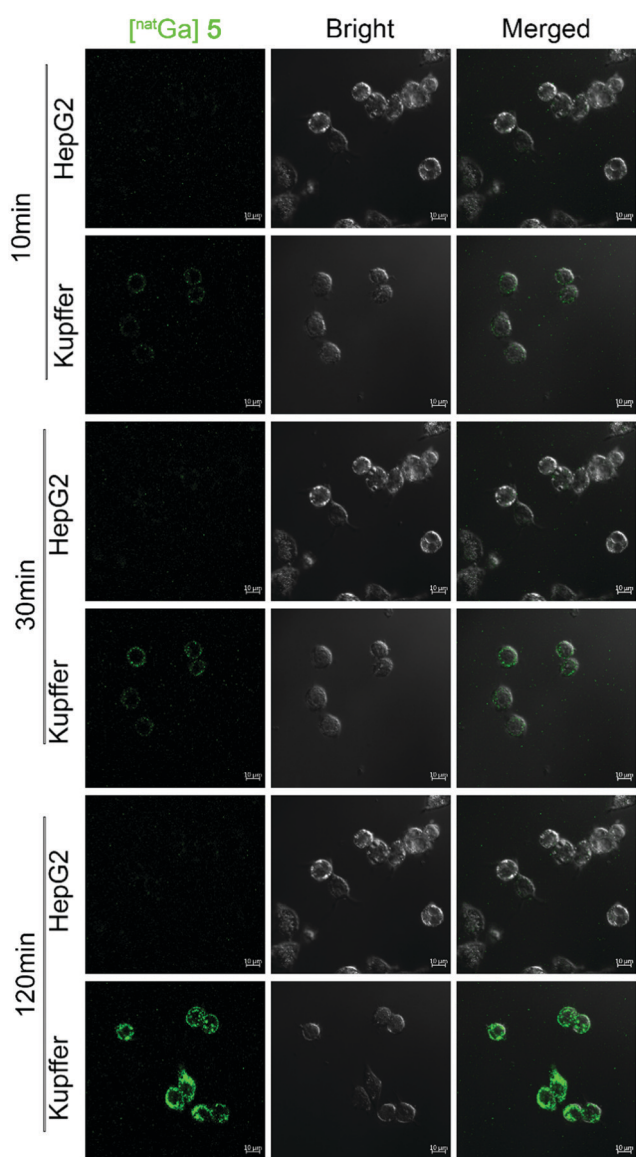


Fig. 4 Confocal images of HepG2 cells and Kupffer cells stained with [^{nat}Ga] 5 conc. = 2 μM, incubation time 10, 30 and 120 min, excitation wavelength: 405 nm; emission filter: 460–520 nm.

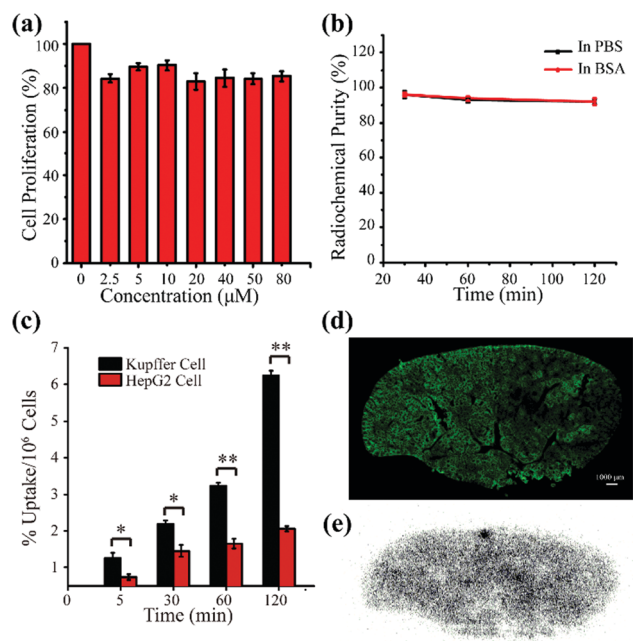


Fig. 5 (a) Relative Cell proliferation of Kupffer cells after treating with [^{68}Ga] **5** with the concentration of **Y** ranging from 2 to 10 μM for 24 h. No significant difference was observed after the addition of [^{68}Ga] **5** compared with the control group ($P > 0.05$). (b) The stability in PBS and plasma of [^{68}Ga] **5**. (c) *In vitro* cell uptake of [^{68}Ga] **5**. The two cell was compared using two-tailed *t* tests (*, $P < 0.01$ and **, $P < 0.001$). Each data point represents mean \pm SD from five trails. The fluorescence images (d) and *in vitro* autoradiography (e) of liver sections from mice injection of [^{68}Ga] **5** into mice.

Table 1 *In vivo* biodistribution of [^{68}Ga] **5** in rats

Organ	5 min	30 min	60 min	120 min
Brain	0.41 \pm 0.1	0.21 \pm 0.2	0.09 \pm 0.01	0.15 \pm 0.05
Liver	13.21 \pm 3.27	14.49 \pm 2.3	16.37 \pm 0.69	20.65 \pm 2.2
Heart	0.62 \pm 0.06	0.28 \pm 0.17	0.2 \pm 0.02	0.25 \pm 0.05
Spleen	5.83 \pm 0.51	5.72 \pm 0.29	5.3 \pm 0.56	6.75 \pm 1.13
Lung	1.75 \pm 0.21	1 \pm 0.25	1.49 \pm 0.41	1.03 \pm 0.28
Kidney	0.37 \pm 0.04	0.26 \pm 0.22	0.17 \pm 0.01	0.2 \pm 0.02
Muscle	1.84 \pm 0.76	0.33 \pm 0.19	0.31 \pm 0.12	0.29 \pm 0.09
Bone	4.39 \pm 0.97	1.13 \pm 0.48	1.04 \pm 0.37	1.51 \pm 0.82
Skin	2.05 \pm 1.36	0.52 \pm 0.08	0.66 \pm 0.2	0.83 \pm 0.24
Blood	5.03 \pm 1.01	3.95 \pm 5.08	3.39 \pm 0.92	3.01 \pm 0.61

The *in vivo* biodistribution results suggested that [^{68}Ga] **5** is mainly taken up by the liver, which is consistent with the cellular fluorescence imaging and cellular uptake results.

1.29 MBq of [^{68}Ga] **5** was administrated *via* tail vein injection without anesthesia. The animals were euthanized at 5, 30, 60, 120 min ($n = 5$) after injection. The data are expressed as mean % ID per g with standard deviation. There was significant difference in tumor and muscle uptake values after 5 min ($p < 0.001$), 30 min ($p < 0.001$), 60 min ($p < 0.0001$), and 120 min ($p < 0.001$) of injection.

3.9 MicroPET imaging

Dynamic small-animal PET studies on rats were performed with [^{68}Ga] **5**. Animal PET images of summed 2 h coronal sections were selected for visualization. As the images demonstrate,

clear liver uptake is visualized, and other organs did not see significant intake (Fig. 6a–c and Fig. S8, ESI †). To confirm this, region of interest analysis was performed using Amira 3.1 image visualization and analysis software on the reconstructed images to generate the time–activity curves for [^{68}Ga] **5**. The kinetics indeed confirm that the tracer exhibited higher liver uptake than muscle (background) region uptake. Rapid liver uptake is visualized within the first 5 min. Liver uptake remains rather consistent throughout the 2 h scan time, with an observed slow washout rate (Fig. 6d). As shown in Fig. S3 (ESI †), the circulation lifetime of [^{68}Ga] **5** in the blood is very short, which may be because [^{68}Ga] **5** forms nanoparticles larger than 100 nm in the blood, which is not conducive to blood circulation.^{37,38} Nanoparticles (> 100 nm) may be particularly trapped in macrophages of the reticuloendothelial system (RES),^{37,38} which may be an important reason for the high uptake of [^{68}Ga] **5** by the liver. [^{68}Ga] **5** was phagocytosed by Kupffer cells when blood flows into the liver, thereby achieving the purpose of liver function imaging. Since hepatic metastases lack Kupffer cells, they would not show uptake after [^{68}Ga] **5** administration, therefore, there is no signal or weak signal in the liver lesions compared with normal liver function PET imaging. However, focal liver lesions with Kupffer cells, such as focal nodular hyperplasia, adenoma, and well-differentiated hepatocellular carcinoma, will show significant uptake,¹⁵ therefore, the liver lesions signal was enhanced compared with normal liver function pet imaging. Based on the results we obtained and by comparing the data from previously reported liver imaging agents and TPE derivatives,^{13,15,39,40} [^{68}Ga] **5** is expected to be a promising PET imaging agent for liver functional imaging.

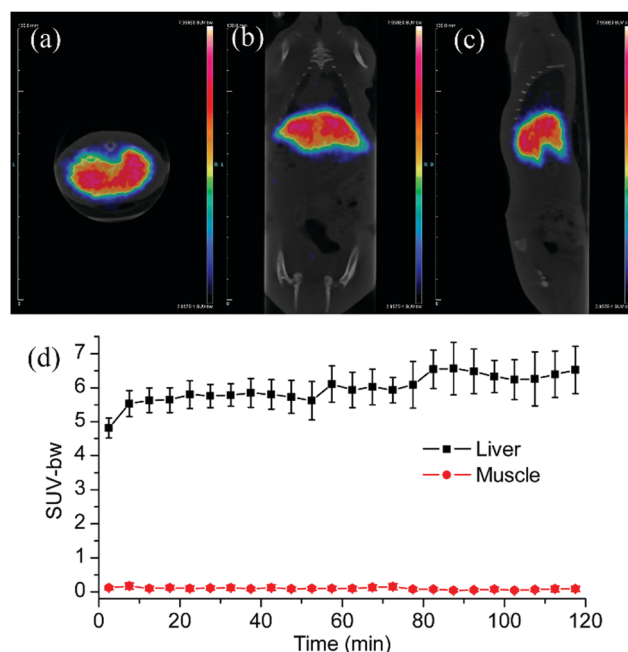


Fig. 6 Representative PET images of rats after intravenous injection of [^{68}Ga] **5**. The images of the (a) transverse, (b) coronal, and (c) sagittal views are from a summed 2 h scan. (d) Time–activity curves of [^{68}Ga] **5** uptake in the liver and muscle.

4. Conclusions

In this work, the integration of fluorophores and complexing agents reduces the influencing factors of multimodal imaging agent design, which strongly promotes the development of PET-FL multimodal imaging agents. The bifunctional complexing agent with AIE characteristics designed in this paper has a wider range of labelling pH values and milder labelling conditions than HBED-CC and is suitable for the labelling of sensitive peptides or antibodies. In addition, $^{68}\text{Ga}^{3+}$ provides a simple, rapid radiolabelling method, which is suitable for use in a convenient lyophilized kit formulation. In summary, this work designed an AIE-based PET liver function imaging agent. $[\text{nat}^{68}\text{Ga}] \mathbf{5}$ can form nanoscale micelles in $\text{DMSO}/\text{H}_2\text{O} = 1/99$. These nanoaggregates have high emissivity and exhibit a typical AIE effect. Fluorescence imaging experiments and radioactivity uptake experiments showed that Kupffer cells had high uptake of $[\text{nat}^{68}\text{Ga}] \mathbf{5}$, while HepG2 cells had lower uptake of $[\text{nat}^{68}\text{Ga}] \mathbf{5}$. $[\text{nat}^{68}\text{Ga}] \mathbf{5}$ has simple labelling conditions, high stability *in vivo*, and enters and accumulates in the liver through phagocytosis by Kupffer cells after intravenous injection into rats. Biodistribution and small animal PET/CT studies showed that $[\text{nat}^{68}\text{Ga}] \mathbf{5}$ shows a high uptake in the liver after intravenous injection. Therefore, PET imaging of $[\text{nat}^{68}\text{Ga}] \mathbf{5}$ can be used to evaluate liver function, locate liver lesions, and then guide fluorescent removal of the lesions, which is important for the clinical diagnosis, treatment and postoperative evaluation of liver disease. Based on this work, PET probes with red AIE characteristics that target different diseases and complex radioactive metals are being synthesized in our laboratory to enhance *in vivo* PET and fluorescence imaging as well as radioactive targeted therapy.

Conflicts of interest

There are no conflicts to declare.

Acknowledgements

This research was supported by the National Natural Science Foundation of China (81701753) and Scientific Research Common Program of Beijing Municipal Commission of Education (KM201810025021). We thank Professor Kung Hank F., Professor Zhu Lin and all members of their team. We also acknowledge Core Facility Center of Capital Medical University and Capital Medical University Beijing Anzhen Hospital PET Center.

Notes and references

- 1 T. Muller, S. Mehrle, A. Schieck, U. Haberkorn, S. Urban and W. Mier, *Mol. Pharmaceutics*, 2013, **10**, 2230.
- 2 N. D. Shah, M. Ventura-Cots, J. G. Abraldes, M. Alborai, A. Alfadhli, J. Argemi, E. Badia-Aranda, E. A. Soler, A. S. T. Barritt, F. Bessone, M. Biryukova, F. J. Carrilho, M. C. Fernandez, Z. D. Guiridi, M. El Kassas, T. Eng-Kiong, A. Farias, J. George, W. Gui, P. Harichander-Thurairajah, J. C. Hsiang, A. Husic-Selimovic, V. Isakov, M. Karoney, W. Kim, J. Kluwe, R. Kochhar, N. Dhaka, P. M. Costa, M. A. Nabeshima Pharm, S. K. Ono, D. Reis, A. Rodil, C. R. Domech, F. Saez-Royuela, C. Scheurich, W. Siow, N. Sivac-Burina, E. S. Dos Santos Traquino, F. Some, S. Spreckic, S. Tan, J. Vorobioff, A. Wandera, P. Wu, M. Yakoub, L. Yang, Y. Yu, N. Zahiragic, C. Zhang, H. Cortez-Pinto and R. Bataller, *Clin. Gastroenterol. Hepatol.*, 2019, **29**, 30073.
- 3 P. Schmeltzer and K. E. Sherman, *Dig. Dis. Sci.*, 2010, **55**, 3328.
- 4 S. P. Georgiadou, K. Zachou, C. Liaskos, S. Gabeta, E. I. Rigopoulou and G. N. Dalekos, *Liver Int.*, 2009, **29**, 434.
- 5 J. Zhou, Z. Wang, S. J. Qiu, X. W. Huang, J. Sun, W. Gu and J. Fan, *J. Cancer Res. Clin. Oncol.*, 2010, **136**, 1453.
- 6 J. Belghiti and D. Fuks, *Liver Cancer*, 2012, **1**, 71.
- 7 K. Hasegawa, N. Kokudo and M. Makuuchi, *Saudi. Med. J.*, 2007, **28**, 1171.
- 8 P. Bharti, D. Mittal and R. Ananthasivan, *Ultrason Imaging*, 2017, **39**, 33.
- 9 T. Tajima, K. Yoshimitsu, H. Irie, A. Nishie, M. Hirakawa, K. Ishigami, Y. Ushijima, D. Okamoto and H. Honda, *Acta Radiol.*, 2009, **50**, 743.
- 10 D. R. Martin and R. C. Semelka, *Semin Ultrasound CT MR*, 2005, **26**, 116.
- 11 D. R. Vera, K. A. Krohn, R. C. Stadalnik and P. O. Scheibe, *J. Nucl. Med.*, 1984, **25**, 779.
- 12 R. Haubner, A. M. Schmid, A. Maurer, C. Rangger, L. G. Roig, B. J. Pichler and I. J. Virgolini, *Mol. Imaging Biol.*, 2017, **19**, 723.
- 13 R. Haubner, D. R. Vera, S. Farshchi-Heydari, A. Helbok, C. Rangger, D. Putzer and I. J. Virgolini, *Eur. J. Nucl. Med. Mol. Imaging*, 2013, **40**, 1245–1255.
- 14 W. de Graaf, R. J. Bennink, R. Vetelainen and T. M. van Gulik, *J. Nucl. Med.*, 2010, **51**, 742–752.
- 15 Y. Chen, M. Li, Y. Hong, J. W. Lam, Q. Zheng and B. Z. Tang, *ACS Appl. Mater. Interfaces*, 2014, **6**, 10783–10791.
- 16 E. Ranyuk, R. Lebel, Y. Bérubé-Lauzière, K. Klarskov, R. Lecomte, J. E. van Lier and B. Guérin, *Bioconjugate Chem.*, 2013, **24**, 1624–1633.
- 17 A. Louie, *Chem. Rev.*, 2010, **110**, 3146–3195.
- 18 D. Patel, A. Kell, B. Simard, B. Xiang, H. Y. Lin and G. Tian, *Biomaterials*, 2011, **32**, 1167–1176.
- 19 L. Sun, J. Ding, W. Xing, Y. Gai, J. Sheng and D. Zeng, *Bioconjugate Chem.*, 2016, **27**, 1200.
- 20 T. K. Förster and K. Ein, *Z. Phys. Chem.*, 1954, 275.
- 21 L. Perk, G. Visser, M. Budde, M. Vosjan, P. Jurek, G. Kiefer and G. van Dongen, *Facile radiolabeling of monoclonal antibodies and other proteins with zirconium-89 or gallium-68 for PET imaging using p-isothiocyanatobenzyl-desferrioxamine*, Nature Publishing Group, 2008.
- 22 J. Mei, N. L. Leung, R. T. Kwok, J. W. Lam and B. Z. Tang, *Chem. Rev.*, 2015, **115**, 11718–11940.
- 23 X. Li, M. Jiang, J. W. Y. Lam, B. Z. Tang and J. Y. Qu, *J. Am. Chem. Soc.*, 2017, **139**, 17022.
- 24 P. Zhang, Z. Zhao, C. Li, H. Su, Y. Wu, R. T. K. Kwok, J. W. Y. Lam, P. Gong, L. Cai and B. Z. Tang, *Anal. Chem.*, 2018, **90**, 1063.

- 25 N. Alifu, A. Zebibula, J. Qi, H. Zhang, C. Sun, X. Yu, D. Xue, J. W. Y. Lam, G. Li, J. Qian and B. Z. Tang, *ACS Nano*, 2018, **12**, 11282.
- 26 C. W. Leung, Y. Hong, S. Chen, E. Zhao, J. W. Lam and B. Z. Tang, *J. Am. Chem. Soc.*, 2013, **135**, 62.
- 27 R. Zhang, S. H. P. Sung, G. Feng, C. J. Zhang, Kenry, B. Z. Tang and B. Liu, *Anal. Chem.*, 2018, **90**, 1154.
- 28 L. Cheng, A. Kamkaew, H. Sun, D. Jiang, H. F. Valdovinos, H. Gong, C. G. England, S. Goel, T. E. Barnhart and W. Cai, *ACS Nano*, 2016, **10**, 7721.
- 29 J. Mei, Y. Huang and H. Tian, *ACS Appl. Mater. Interfaces*, 2018, **10**, 12217.
- 30 C. Han, S. Jiang, J. Qiu, H. Guo and F. Yang, *New J. Chem.*, 2019, **43**, 3317.
- 31 Q. Jiang, Y. Xu, T. Yu, X. Qiu, R. Zhao, D. Zhao, N. Zheng, D. Hu, Z. Xie and Y. Ma, *New J. Chem.*, 2019, **43**, 6721.
- 32 P. A. A. M. Vaz, J. Rocha, A. M. S. Silva and S. Guieu, *New J. Chem.*, 2016, **40**, 8198.
- 33 Y. Ooyama, M. Sugino, T. EnoKi, K. Yamamoto, N. Tsunoji and J. Ohshita, *New J. Chem.*, 2017, **41**, 4747.
- 34 J. Luo, Z. Xie, J. W. Lam, L. Cheng, H. Chen, C. Qiu, H. S. Kwok, X. Zhan, Y. Liu, D. Zhu and B. Z. Tang, *Chem. Commun.*, 2001, 1740.
- 35 A. Roivainen, T. Tolvanen, S. Salomaki, G. Lendvai, I. Velikyan, P. Numminen, M. Valila, H. Sipila, M. Bergstrom, P. Harkonen, H. Lonnberg and B. Langstrom, *J. Nucl. Med.*, 2004, **45**, 347.
- 36 Z. Zha, J. Song, S. R. Choi, Z. Wu, K. Ploessl, M. Smith and H. Kung, *Bioconjugate Chem.*, 2016, **27**, 1314.
- 37 W. Hou, F. Xia, C. S. Alves, X. Qian, Y. Yang and D. Cui, *ACS Appl. Mater. Interfaces*, 2016, **8**, 1447.
- 38 Q. Chen, X. Wang, C. Wang, L. Feng, Y. Li and Z. Liu, *ACS Nano*, 2015, **9**, 5223.
- 39 J. Choi, J. M. Jeong, B. C. Yoo, M. K. Hong, Y. J. Kim, Y. S. Lee, D. S. Lee and J. K. Chung, *Nucl. Med. Biol.*, 2015, **42**, 53.
- 40 C. Tsopelas and W. Hsieh, *J. Labelled Compd. Radiopharm.*, 2017, **60**, 528.